INDUCED SEISMICITY

A risk-based approach for managing hydraulic fracturing–induced seismicity

Ryan Schultz*, Gregory C. Beroza, William L. Ellsworth

Risks from induced earthquakes are a growing concern that needs effective management. For hydraulic fracturing of the Eagle Ford shale in southern Texas, we developed a risk-informed strategy for choosing red-light thresholds that require immediate well shut-in. We used a combination of datasets to simulate spatially heterogeneous nuisance and damage impacts. Simulated impacts are greater in the northeast of the play and smaller in the southwest. This heterogeneity is driven by concentrations of population density. Spatially varying red-light thresholds normalized on these impacts [moment magnitude (M_w) 2.0 to 5.0] are fairer and safer than a single threshold applied over a broad area. Sensitivity tests indicate that the forecast maximum magnitude is the most influential parameter. Our method provides a guideline for traffic light protocols and managing induced seismicity risks.

The injection of fluids into the subsurface has the potential to reactivate critically stressed faults (*1*). In particular, hydraulic fracturing has been recognized as a source of induced earthquakes (*2*), with potentially induced events as large as local magnitude (M_L) 5.7 causing substantial damage (*3*). Although these earthquakes are rare (*4*), the perceived risks of hydraulic fracturing have both caused public concern and impeded industry development (*5*, *6*). Often, traffic light protocols have been used to manage the risks of induced earthquakes (table S1) (*7*, *8*). Many unresolved questions remain about the efficacy of these protocols.

Recent work has better defined traffic light protocols (*9*–*14*), some within a risk-based framework (*15*). We define the red light as the threshold requiring immediate shut-in of the well that is causing the earthquakes. The red-light magnitude is thus chosen to minimize the risks of unacceptable shaking from post–shut-in seismicity (or continued operations). A magnitude threshold for the red light is simple to implement, and forecast modeling can tie those thresholds to risk-based targets of consequence (*15*). Hazards related to ground-motion nuisance and building damage are important considerations, particularly when hydraulic fracturing occurs in low-seismicity regions, where the population may be unfamiliar with or unprepared for earthquake shaking (*2*).

On the basis of this rationale, we developed a risk-based, red-light–threshold approach for the Eagle Ford shale play in Texas (*16*). The Eagle Ford formation has hosted some of the largest confirmed cases of hydraulic fracturing–induced earthquakes in the United States (*17*), albeit somewhat complicated by also having substantial extraction-related seismicity (*18*). Many of the requisite seismological datasets

Department of Geophysics, Stanford University, Stanford, CA, USA.
*Corresponding author. Email: rjs10@stanford.edu

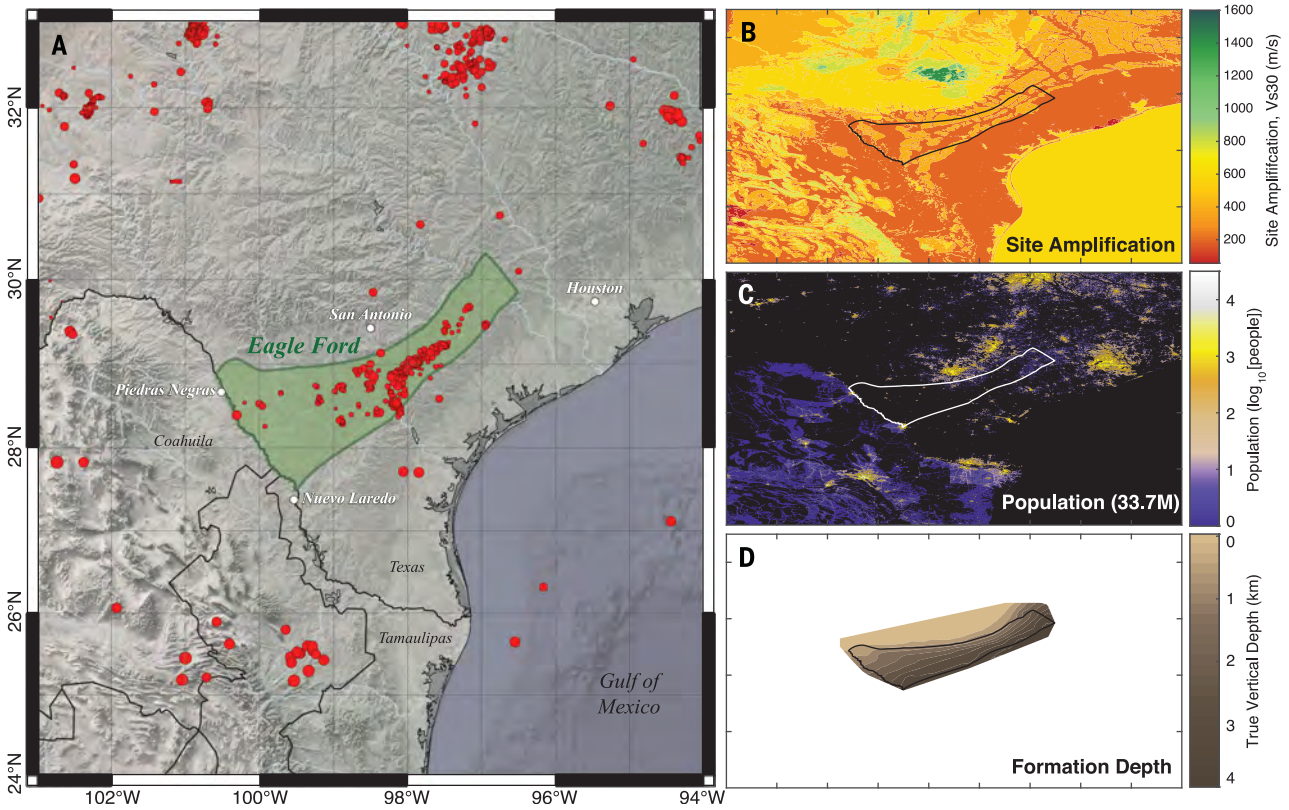

Fig. 1. Maps of spatial information, with the Eagle Ford boundaries. (**A**) Locations of earthquakes (red circles) and the boundaries of the Eagle Ford (green area) are shown alongside political boundaries and municipalities (white circles) for geographic context. (**B**) The same map bounds displaying a proxy for near–surface-site amplification (Vs30, scaled by color). (**C**) The same map bounds displaying the local population counts (log scaled by color, with black denoting zero population). (**D**) The same map bounds displaying the true vertical depth to the Eagle Ford formation (scaled by color).

are available (*19*), and the formation's slender outline transitions through a variety of population densities (Fig. 1 and figs. S1 to S3). For most of these reasons, the Eagle Ford provides an ideal example to illustrate probabilistic red-light thresholds to manage induced earthquake risks.

We gathered publicly available information on earthquake ground motion–prediction equations (*20*), proxies for site amplification of ground shaking (*21*), functions for translating ground-motion intensities to the probabilities of being felt or damaging (*22*, *23*), and spatial distributions of population (*24*) to perform our analysis. Briefly, the workflow that we used simulates the largest induced earthquake trailing the shut-in of a hydraulic fracturing operation, including the event that initially triggered the red light (*25*–*27*). These trailing events are simulated over a range of red-light stopping magnitudes and all possible well locations within the Eagle Ford formation (Fig. 2A). From these simulations, we estimated the number of households that would likely be impacted by nuisance or damaging ground motions (Fig. 2B), similar to fatality estimates after an earthquake (*28*). Many of the input parameters to this problem have noteworthy variabilities (fig. S6), so we used a 300-trial Monte Carlo sample to represent earthquake impacts as a statistical distribution (*15*, *29*). Stopping at a larger-magnitude red light increases the number of impacted households; however, the number of households impacted can vary spatially (Fig. 2C), with the more densely populated areas in the northeast of the Eagle Ford (near Karnes City, San Antonio, and Houston) producing greater impacts. Although these impacts are spatially heterogeneous, the variabilities between individual realizations are far more pronounced (e.g., Fig. 2, B versus C). In this sense, we can design traffic light protocols that spatially vary to account for this controllable factor and then set risk tolerances that account for the uncontrollable factors.

This spatial heterogeneity of hydraulic fracturing–induced earthquake risks suggests that single-valued red-light magnitudes for an entire play are likely unfair: either too restrictive in rural areas (incurring unnecessary costs for operators) or too permissive near urban areas (potentially incurring inadequate safety). To address this issue, we preselected acceptable tolerances for nuisance or damage and then estimated the red-light stopping magnitude that would be required to meet them (e.g., Fig. 2C). For the purpose of demonstration, we chose an iso-nuisance tolerance of a 50% chance of 300,000 households being impacted by a community decimal intensity (CDI) of 3. CDI is a questionnaire-based measure that quantifies the degree of earthquake shaking felt by a person (*30*), with levels 2 to 6 roughly corresponding to the subjective criteria of just felt, exciting, somewhat frightening, frightening, and extremely frightening, respectively. Our nuisance tolerance was chosen to keep the number of exciting (CDI 3) felt reports at a manageable level [because only ~0.2% of the population reports their experience (*23*)]. We chose an iso-damage tolerance of a 50% chance of 30 households being impacted at a damage state (DS) of 1. DS is a measure that quantifies the degree of building damage received from earthquake shaking, with levels 1 to 4 corresponding to damage that is slight or minor, moderate, extensive, and complete, respectively. This damage tolerance was chosen to minimize the chances that even cosmetic damage (DS 1) would occur. These tolerance choices are subjective value judgments. In practice, tolerances should be selected on the basis of input from all stakeholders (figs. S8 to S11).

We applied our methodology on the basis of these tolerances for nuisance and damage. Similar to the conceptual results, the number of households impacted by nuisance (given a

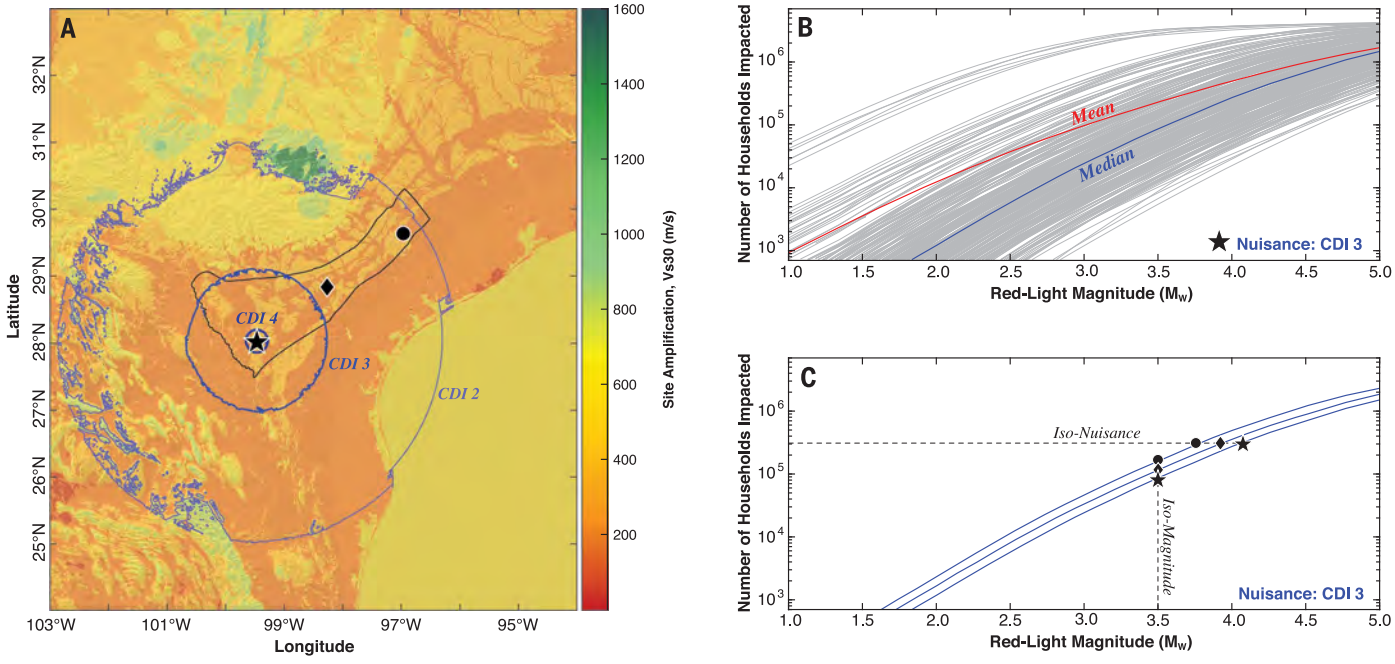

Fig. 2. The concepts of risk-based traffic light protocols. (**A**) Contours of 50% chance of felt ground motion at various nuisance degrees (blue circles and CDI labels) are estimated for a hypothetical induced earthquake (black star) in the Eagle Ford (black lines). A background map of site amplification (Vs30, colored area) provides context for deviations from circularity. The hypothetical ground motions can be computed for various geographic locations (star, diamond, and circle). Not visible, but the contours of 50% chance of encountering building DSs are also plotted underneath the star label. (**B**) Monte Carlo realizations of nuisance impacts at the CDI 3 level (gray lines) and the star location. The median (blue line) and mean curves (red line) may be produced from this distribution of realizations. (**C**) Median curves of nuisance impact (blue lines) for the three hypothetical induced earthquake locations on the left map (star, diamond, circle). Example iso-nuisance and iso-magnitude lines (dashed lines) depict the differing amount of median nuisance impact at the three locations.

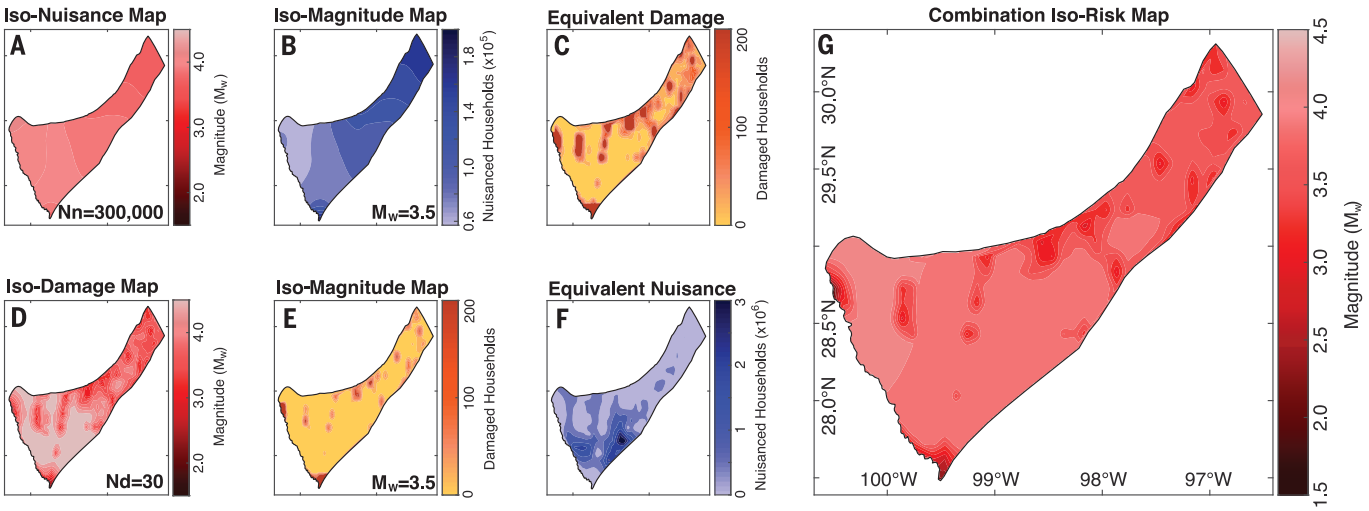

Fig. 3. Red-light impact maps. (**A**) Keeping a tolerance of a 50% chance of impacting 300,000 households at a nuisance level of CDI 3 constant, red-light stopping magnitudes are spatially estimated. (**B**) Keeping a red-light magnitude threshold of M_w 3.5, the median number of households impacted by nuisance at the CDI 3 level is estimated. (**C**) If the map produced in (A) is used as a red-light threshold, the median number of households impacted by damage at the DS 1 level is estimated (capped at 200). (**D**) Keeping a tolerance of a 50% chance of impacting 30 households at a damage level of DS 1 constant, red-light stopping magnitudes are spatially estimated. (**E**) Keeping a red-light magnitude threshold of M_w 3.5, the median number of households impacted by damage at the DS 1 level is estimated (capped at 100). (**F**) If the map produced in (D) is used as a red-light threshold, the median number of households impacted by nuisance at the CDI 3 level is estimated. (**G**) A combination of the two iso-risk maps (A and D), keeping the smaller magnitude at each grid pixel. *N*d, number of households impacted by damage; *N*n, number of households impacted by nuisance.

single-valued red-light threshold) increases toward the more densely populated northeast Eagle Ford formation (Fig. 3B). Nuisance impacts are spatially coherent, with a wavelength on the order of hundreds of kilometers, because moderate magnitude earthquakes are felt at these epicentral distances. Correspondingly, our iso-nuisance approach allows for higher red-light magnitudes of M_w 4.1 in the southwest that reduce to M_w 3.7 in the northeast (Fig. 3A). However, simply using the iso-nuisance magnitudes still produces heterogeneous damage impacts (Fig. 3C).

To explore these heterogeneous damage impacts, we repeated the methodology for damage. The number of households impacted by damage (given a single-valued red-light threshold) generally increases toward the northeast (Fig. 3E). However, this observation generally has a smaller wavelength, on the order of 1 to 10 km. This reflects the localized damage footprint of moderate magnitude earthquakes (*31*, *32*). This creates "pockmark" features of lower red-light magnitudes (M_w ~3.0) in the iso-damage approach (Fig. 3D), which correspond to smaller-town locations (<300,000 households: e.g., Carrizo Springs, Cotulla, and Pearsall) that the iso-nuisance approach tends to miss. The southernmost and westernmost tips of the Eagle Ford have a lower red-light threshold of M_w ~2.0 where they encroach on the nearby Mexican cities of Nuevo Laredo and Piedras Negras. Selecting a red-light magnitude on the basis of iso-damage alone produces heterogeneous nuisance impacts, especially in the sparsely populated southwestern area, where damage is unlikely (with red-light magnitudes up to M_w 5.0); however, allowing earthquakes of this magnitude has the potential to jeopardize the social license to operate (*5*).

To accommodate the shortcomings of either iso-risk approach, we produced a combination map. At every grid pixel, we take the smaller red-light magnitude between the iso-nuisance (Fig. 3A) and iso-damage maps (Fig. 3D). This combination map (Fig. 3G) ensures that neither the prescribed nuisance nor damage tolerances will be exceeded. In general, the sparsely populated rural areas tend to be controlled by the iso-nuisance tolerances, whereas iso-damage tolerances are more important in urban regions. The spatially averaged red-light magnitude is M_w 3.8 for this map.

We further tested the accuracy of our impact estimates and the level of restrictions our combination map would have imposed on operators. We retrospectively note that this combination map would have encountered four red-light earthquakes (e.g., M_w 4.8, 20 October 2011; fig. S12), on the basis of Eagle Ford's history of seismicity (*17*, *18*). These four earthquakes were previously related to petroleum extraction (*18*). The statistics reported for these red-light earthquakes (~50% felt at CDI 3+) are very similar to the tolerance we selected (fig. S13), providing some justification of our results. However, the retrospective analysis changes appreciably, depending on the tolerance for risk selected (figs. S8 to S11): Red lights for our most risk-tolerant and risk-averse choices range between 1 and 28 earthquakes (fig. S12). In regions where prior seismicity has occurred, these types of retrospective analyses could be used to inform risk tolerance choices.

Communities may have differing tolerances to nuisance or damage (*15*), and our approach provides useful guidelines for choosing traffic light thresholds. Our approach probabilistically defines red-light thresholds in a risk-based manner by combining nuisance and damage consequences while keeping magnitude-based red lights (which are simple to implement). Discretized versions of the combination map could also be used for further implementational simplicity (fig. S14). The yellow-light threshold (the point at which operator mitigation begins) could be defined based on the red-light threshold (e.g., M_w 2.0 lower than red) to minimize the number of green-to-red jumps encountered (*15*). Although this approach has been applied to the entire footprint of the Eagle Ford, only the susceptible regions that actually encounter earthquakes (*33*) would require management. Additionally, our approach could easily be adapted to hydraulic fracturing plays worldwide (*2*). Although this approach has been applied to hydraulic

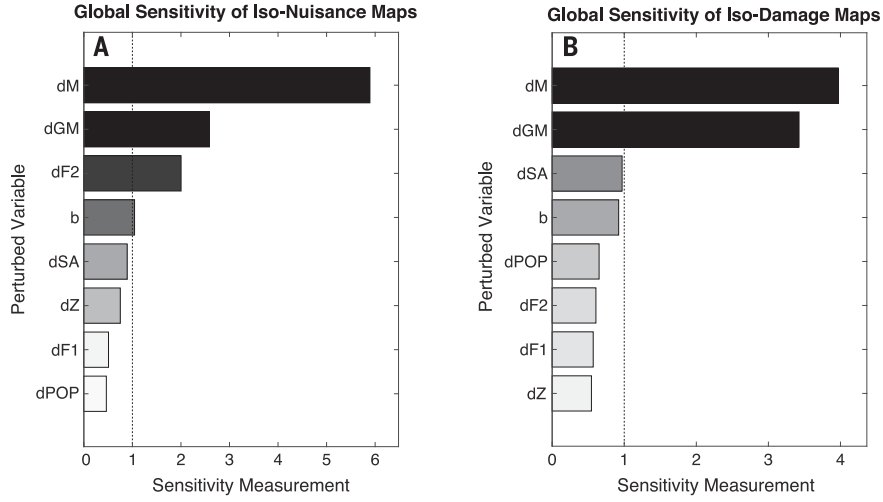

Fig. 4. Sensitivity plots. (**A** and **B**) Sensitivity of perturbed input parameters on the output iso-risk results (A) for the iso-nuisance map and (B) for the iso-damage map. Values above the 95% confidence interval (dashed line) are notably influential parameters. Labels on the *x* axis are abbreviated as follows: b, *b*-value; dF1 and dF2, nuisance/fragility function covariances; dGM, ground-motion–prediction equation uncertainty; dM, forecast magnitude perturbation; dSA, site amplification perturbation; dPOP, population perturbation; dZ, earthquake depth perturbation.

fracturing–induced seismicity, it would be applicable to induced earthquake risk in other settings, such as enhanced geothermal projects, or any other cases of induced seismicity with a quantifiable link between the causal operations and the induced sequence.

We acknowledge that this approach is subject to a number of variabilities and assumptions in our modeling (*15*). Many of these have the potential to change the simulated nuisance or damage impacts (e.g., Fig. 2B). Because of this, we used a statistical approach (*34*) to quantify the sensitivity of the output iso-nuisance and iso-damage results to the variable perturbations in the Monte Carlo analysis (Fig. 4). We found that the forecast maximum magnitude is the most influential parameter, followed by ground motion–prediction uncertainties, for both of the iso-risk maps. The sensitivity tests for the iso-nuisance map also suggest that perturbations to the nuisance likelihood function have an influence on the iso-nuisance map. All remaining parameters appear to have a minor influence on the resulting iso-maps. We interpret this ranking of parameter influences as a suggested order of research priorities; i.e., to better constrain red-light thresholds (and thus constrain induced earthquake risks), better models of the largest earthquakes after a well shut-in are needed the most (*27*). Accurate and regionally calibrated ground-motion predictions are also important, especially when considering damage impacts (Fig. 4B).

We have built a generalized approach to set red-light magnitude thresholds for managing the risks of hydraulic fracturing–induced seismicity. These thresholds are informed by simulated impacts of nuisance and damage. Furthermore, we applied this approach to the earthquakes induced in the Eagle Ford shale play. Although we have made particular risk tolerance choices in this paper to illustrate the methodology, communities, regulators, or operators would be expected to tailor tolerances according to their needs. Sensitivity tests indicate that better forecast models of earthquakes after the shut-in of a well and suitably calibrated ground motion–prediction equations are among the most important factors to improve. This approach to designing red-light thresholds in traffic light protocols will likely be useful for other cases of induced seismicity, such as enhanced geothermal systems.

REFERENCES AND NOTES

1. W. L. Ellsworth, *Science* **341**, 1225942 (2013).
2. R. Schultz *et al.*, *Rev. Geophys.* **58**, e2019RG000695 (2020).
3. X. Lei, Z. Wang, J. Su, *Seismol. Res. Lett.* **90**, 1099–1110 (2019).
4. G. M. Atkinson *et al.*, *Seismol. Res. Lett.* **87**, 631–647 (2016).
5. D. C. Smith, J. M. Richards, *Oil Gas Nat. Resour. Energy J.* **1**, 81–163 (2015).
6. H. Ghofrani, G. M. Atkinson, R. Schultz, K. Assatourians, *Seismol. Res. Lett.* **90**, 1420–1435 (2019).
7. J. J. Bommer *et al.*, *Eng. Geol.* **83**, 287–306 (2006).
8. M. D. Zoback, *Earth Mag.* **57**, 38 (2012).
9. J. Douglas, H. Aochi, *Pure Appl. Geophys.* **171**, 1847–1858 (2014).
10. A. Mignan, D. Landtwing, P. Kästli, B. Mena, S. Wiemer, *Geothermics* **53**, 133–146 (2015).
11. A. Mignan, M. Broccardo, S. Wiemer, D. Giardini, *Sci. Rep.* **7**, 13607 (2017).
12. S. Baisch, C. Koch, A. Muntendam-Bos, *Seismol. Res. Lett.* **90**, 1145–1154 (2019).
13. C. Langenbruch, W. L. Ellsworth, J. U. Woo, D. J. Wald, *Geophys. Res. Lett.* **47**, e2019GL085878 (2020).
14. G. Cremen, M. J. Werner, *Nat. Hazards Earth Syst. Sci.* **20**, 2701–2719 (2020).
15. R. Schultz, G. Beroza, W. Ellsworth, J. Baker, *Bull. Seismol. Soc. Am.* **110**, 2411–2422 (2020).
16. US Energy Information Administration, "Updates to the EIA Eagle Ford Play Maps" (US Department of Energy, 2014); www.eia.gov/maps/pdf/eagleford122914.pdf.
17. S. L. Fasola *et al.*, *Geophys. Res. Lett.* **46**, 12958–12967 (2019).
18. C. Frohlich, M. Brunt, *Earth Planet. Sci. Lett.* **379**, 56–63 (2013).
19. A. Savvaidis, B. Young, G. C. D. Huang, A. Lomax, *Seismol. Res. Lett.* **90**, 1702–1715 (2019).
20. G. Zalachoris, E. M. Rathje, *Earthq. Spectra* **35**, 1–20 (2019).
21. D. C. Heath, D. J. Wald, C. B. Worden, E. M. Thompson, G. M. Smoczyk, *Earthq. Spectra* **36**, 570–1584 (2020).
22. Federal Emergency Management Agency (FEMA). "Hazus-MH 2.1" in *Multi-Hazard Loss Estimation Methodology Technical and User Manuals* (Federal Emergency Management Agency, 2015).
23. R. Schultz, V. Quitoriano, D. J. Wald, G. Beroza, *Earthq. Spectra*, 10.1177/8755293020988025 (2021).
24. A. N. Rose, J. McKee, M. L. Urban, E. A. Bright, K. M. Sims, "LandScan 2018 High-Resolution Global Population Data Set" (No. LandScan 2018 High-Resolution Global Population Da; 005854MLTPL00; Oak Ridge National Laboratory, 2019).
25. N. J. van der Elst, M. T. Page, D. A. Weiser, T. H. Goebel, S. M. Hosseini, *J. Geophys. Res. Solid Earth* **121**, 4575–4590 (2016).
26. R. Schultz, G. Atkinson, D. W. Eaton, Y. J. Gu, H. Kao, *Science* **359**, 304–308 (2018).
27. J. P. Verdon, J. J. Bommer, *J. Seismol.* **25**, 301–326 (2021).
28. K. Jaiswal, D. Wald, *Earthq. Spectra* **26**, 1017–1037 (2010).
29. Materials and methods are available as supplementary materials.
30. D. J. Wald, V. Quitoriano, C. B. Worden, M. Hopper, J. W. Dewey, *Ann. Geophys.* **54**, 688–707 (2011).
31. R. E. Chase, A. B. Liel, N. Luco, B. W. Baird, *Earthquake Eng. Struct. Dynam.* **48**, 1365–1383 (2019).
32. B. W. Baird, A. B. Liel, R. E. Chase, *Earthq. Spectra* **36**, 1995–2018 (2020).
33. S. Pawley *et al.*, *Geophys. Res. Lett.* **45**, 1786–1793 (2018).
34. J. Park, G. Yang, A. Satija, C. Scheidt, J. Caers, *Comput. Geosci.* **97**, 15–29 (2016).

ACKNOWLEDGMENTS

We thank two anonymous reviewers whose critiques helped to improve the quality of this manuscript. We also thank J. Baker for pointing us toward datasets and resources. **Funding:** This work was supported by the Stanford Center for Induced and Triggered Seismicity. **Author contributions:** R.S. conceived the project, carried out the analysis, and wrote the manuscript with guidance, comments, and revisions from all of the authors. G.C.B. and W.L.E. supervised the project. **Competing interests:** The authors declare no competing interests. **Data and materials availability:** Site amplification (*21*), population (*24*), Eagle Ford depth (*16*), ground motion predication equation (*20*), nuisance function (*23*), and fragility function (*22*) information are derived from prior studies.

SUPPLEMENTARY MATERIALS

science.sciencemag.org/content/372/6541/504/suppl/DC1
Materials and Methods
Figs. S1 to S15
Tables S1 and S2

12 January 2021; accepted 29 March 2021
10.1126/science.abg5451

A risk-based approach for managing hydraulic fracturing–induced seismicity

Ryan Schultz, Gregory C. Beroza and William L. Ellsworth

Science **372** (6541), 504-507.
DOI: 10.1126/science.abg5451

Varying the stop lights

Traffic light protocols can help to mitigate induced earthquakes from unconventional oil production. However, they are not geographically tuned to account for how shaking may actually translate to structural damage. Schultz *et al.* incorporated damage tolerance into a traffic light protocol for the Eagle Ford shale play. They found that shut-off may be necessary more quickly in populated regions, whereas sparsely populated areas of the play can take up to a magnitude 5 earthquake without issue. This risk-based strategy provides a more nuanced approach to regulating induced seismicity.

Science, this issue p. 504